Microstructural dependence of the thermal and mechanical properties of monazite LnPO$_4$ (Ln = La to Gd)

L. Perrière [a], D. Bregiroux [a,b,*], B. Naitali [c], F. Audubert [a], E. Champion [b], D.S. Smith [c], D. Bernache-Assollant [d]

[a] *Commissariat à l'Energie Atomique, DEN/DEC/SPUA/LTEC, Cadarache, 13108 Saint-Paul-Lez-Durance, France*
[b] *Laboratoire Science des Procédés Céramiques et de Traitement de Surface, UMR CNRS-Université n°6638, 123 avenue Albert Thomas, 87060 Limoges, France*
[c] *Groupe d'Etude des Matériaux Hétérogènes, EA n°3178, ENSCI, 47 avenue Albert Thomas, 87100 Limoges, France*
[d] *Ecole des Mines, CIS, 158 cours Fauriel, 42023 Saint-Etienne cedex, France*

Abstract

In this work are given some thermal and mechanical properties of monazite, related to the microstructure. This compound is a poor thermal conductive ($\lambda < 5$ W m^{-1} K^{-1}), with a thermal expansion in between 9 and 10×10^{-6} K^{-1} according to the considered crystallographic direction, and a relatively high specific heat ($C_p \approx 110$ J mol^{-1} K^{-1}). Mechanical properties of monazite are characteristic of a brittle behavior: bending strength is of about 100 MPa and fracture toughness is close to 1 MPa m$^{1/2}$. Porosity plays a large role on both thermal and mechanical properties pointing out the importance of controlling the whole elaboration process.
© 2007 Elsevier Ltd. All rights reserved.

Keywords: Monazite; Mechanical properties; Thermal properties; Microstructure-final

1. Introduction

One field of research conducted in the framework of the French law of 30 December 1991[1] describing the management of long-lived and high-activity radioactive waste consists in separating the radionuclides in order to perform their specific immobilization. It is then necessary to develop and optimize adapted host matrices for those radionuclides.[2] In this aim, crystalline materials have been investigated.[3] On the basis of geological observations, monazite, a light lanthanide orthophosphate LnPO$_4$ (Ln = La to Gd) is viewed as potential nuclear waste matrix for the specific immobilization of minor actinides (neptunium, americium and curium). Indeed, 2 million years old natural monazite samples have been discovered in Brazil.[4] These samples remained crystalline, showing that

monazite is very resistant against metamictization due to alpha particles.[5] Moreover, the monazite structure can anneal the self-irradiation defects at a relatively low temperature.[6] Another remarkable property of monazite, which makes this material very interesting to be used as a nuclear waste matrix, is its low solubility in water.[7] Despite monazite compounds have been shown as potential radionuclides matrices, complementary studies are necessary to complete the database of those compounds, in particular concerning their mechanical and thermal properties that are important for the concerned application. A few studies have been devoted to the thermal and mechanical properties of LnPO$_4$, especially LaPO$_4$,[3,8–11] but no one described the possible influence of the microstructure. On these bases, this paper deals with the sintering of LnPO$_4$ compounds (Ln = La, Pr, Nd or Eu) and the determination of some of their thermal (specific heat, thermal conductivity, coefficient of thermal expansion) and mechanical (elastic moduli, flexural strength, hardness and fracture toughness) properties. For each property, the eventual microstructure influence will be discussed.

* Corresponding author at: Université Pierre et Marie Curie - Paris 6, CNRS UMR 7574, Chimie de la Matière Condensée de Paris, 4 place Jussieu, Paris F-75005, France. Tel.: +33 144275532; fax: +33 144272548.
E-mail address: damien.bregiroux@ccr.jussieu.fr (D. Bregiroux).

2. Materials and methods

The $LnPO_4$ powders were synthesized by high temperature solid–solid reaction of a pure and anhydrous $La_2O_3/NH_4H_2PO_4$ mixture, according to the experimental protocol described elsewhere.[12] The reaction was completed by two calcinations at 1350 °C for 2 h in air. The monazite structure was confirmed by X-ray diffractometry (Bruker-AXS D8, Germany). In order to increase its reactivity, the powder was ground by dry mixer-milling of batches of 4 g in a zirconia jar using a zirconia ball for 3 cycles of 20 min at an oscillating frequency of 18 Hz. The specific surface area of the ground powder was measured according to the BET method into N_2 (Micromeritics Gemini BET analyser, USA), and was found ranging from 5 to 10 $m^2 g^{-1}$.

Powder was unidirectionally pressed with a pressure of 65 MPa (Hymatec press, France) into pellets of 30 mm in diameter. The pellets were then sintered (Nabertherm furnace, Germany) at 1500 °C for 0.1–20 h in air with a heating and cooling rate of 10 °C min^{-1}.

The density of the sintered pellets was determined by the Archimedean method in water. The relative density was calculated using the absolute density obtained by He pycnometry on the powders. Grain size distribution and average grain size were calculated upon thermally etched (etching was obtained by an annealing at 1450 °C for 6 min) samples using SEM micrographs, according to the equivalent diameter disk method using a commercial software (Analysis, Soft Imaging System, Olympus). A summary of the typical microstructures is given in Fig. 1a–c, showing a relatively homogeneous grain size and an intergranular porosity. Until the relative density of 97%, the grain growth is very low, and, as soon as this value is reached, the grain growth occurs rapidly at constant relative density.

The coefficient of thermal expansion (CTE) was measured by dilatometry (Setaram TMA 92, France) on 2 mm height pellets presenting a relative density close to 98.5%. Samples were heated up to 1000 °C at the rate of 2 °C min^{-1}, and an average value of CTE was calculated in the 200–1000 °C temperature range. In order to subtract the thermal expansion of the experimental device, a blank experiment has been performed. Tests of repeatability were carried out by multiple experiments on the same sample. The dispersion of the results was thus found to be $0.3 \times 10^{-6} K^{-1}$. For $NdPO_4$, lattice parameters thermal expansion was investigated by high-temperature X-ray diffraction (HTXRD) using a Pt–10%Rh strip and MgO as internal standard (the X-ray diffractogram was obtained on a 25/75 weight ratio $MgO/NdPO_4$ powder mix). The specific heat (C_p) measurements were performed on ground powders on a calorimeter Calvet (Setaram C80, France) in the 30–200 °C temperature range, with a heating rate of 0.2 °C min^{-1}. The thermal diffusivity α was measured on 2 mm thick and 10 mm diameter pellets by the flash laser method. Degiovanni's analysis was used to calculate α since heat losses in the experiment are taken into account.[13,14] The thermal conductivity λ was then deduced (Eq. (1)):

$$\lambda = \alpha C_p \rho \tag{1}$$

where ρ is the bulk density of the sample. As obtained with Eq. (1), λ depends on the porosity of the sample. A relation deduced from the Maxwell–Eucken model[15] makes it possible to overcome this effect (Eq. (2)):

$$\lambda_d = \frac{2\lambda^2 - \lambda\lambda_p(3f_p - 1)}{\lambda_p + \lambda(3f_s - 1)} \tag{2}$$

where λ is the calculated thermal conductivity, λ_p the pores one ($\lambda_p = 0.026$ W $m^{-1} K^{-1}$ at room temperature) and λ_d is the thermal conductivity extrapolated to a fully dense sample. f_p and f_s are the volume fractions of pores and solid, respectively. Eq. (3) describes the dependence of λ_d versus grain boundaries[15]:

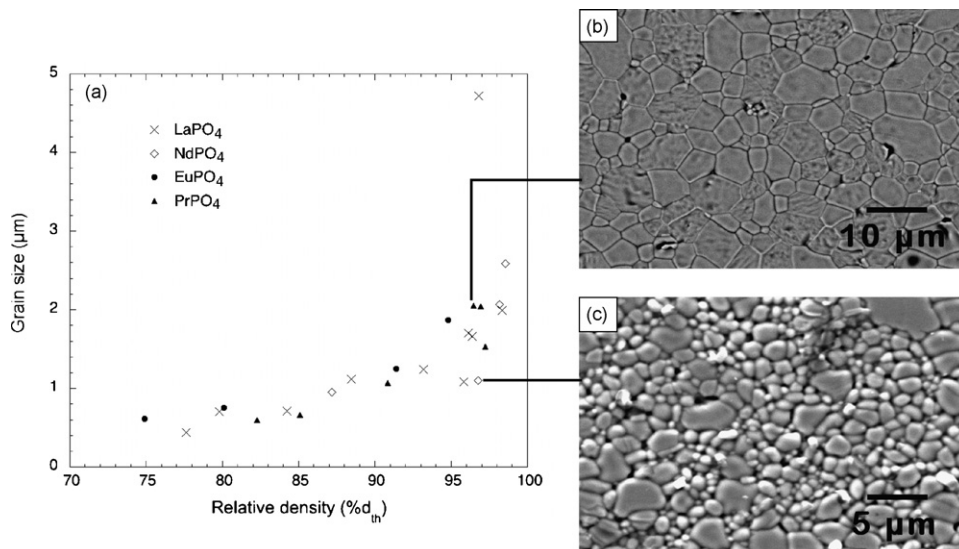$$\frac{1}{\lambda_d} = \frac{1}{\lambda_{sc}} + nR_{gb} \tag{3}$$

Fig. 1. Microstructural map (a) and typical microstructures of: (b) $NdPO_4$ (relative density, 96.8%; grain size, 1.10 μm) and (c) $PrPO_4$ (relative density, 96.5%; grain size, 2.05 μm).

where λ_{sc} is the single-crystal thermal conductivity and R_{gb} is the grain boundaries thermal resistance and n the number of grain boundaries crossed by the heat flow (n is equivalent to the inverse of the grain size).

The elastic moduli were determined on sintered pellets at room temperature from measurements of the longitudinal (V_l) and transverse (V_t) ultrasonic wave velocities, which were determined using two 5 MHz piezoelectric transducers (Ultran, USA). Young's modulus (E), shear modulus (G) and Poisson's ratio (v) were derived from the following equations:

$$V_l = \left[\frac{E(1-v)}{\rho(1-2v)(1+v)}\right]^{1/2} \quad (4)$$

$$V_t = \sqrt{\frac{G}{\rho}} \quad (5)$$

$$v = \left(\frac{E}{2G}\right) - 1 \quad (6)$$

Flexural strength was measured by 3 points bending on mirror polished 15 mm × 5 mm × 4 mm bars using a 12 mm span and a 0.5 mm min^{-1} crosshead speed (Instron 3342).

Vickers Hardness (H_v) and fracture toughness (K_{Ic}) were measured according to the micro-indentation technique (Paars Physics MHT-10) on mirror polished (up to 1 μm) samples. The applied load was 225 g. K_{Ic} is given by the following expression, which is derived from the model proposed by Evans and Charles[16]:

$$K_{Ic} = 0.0824 \frac{F}{c^{3/2}} \quad (7)$$

where F is the indentation load (in Newtons) and c the average length of the induced radial cracks.

3. Results and discussion

3.1. Thermal properties

The linear coefficients of thermal expansion of the different lanthanide phosphates are given in Fig. 2. Values of CTE are between 10 and 11.5×10^{-6} K^{-1}, which is a relatively wide range of variation, but rather low compared to other potential minor actinides host matrices such as neodymium substituted britholite (21×10^{-6} K^{-1})[17] or hydroxyapatite (16×10^{-6} K^{-1}).[18] The average value of CTE seems to increase with the atomic number of the lanthanide element, i.e. when the ionic radius of the rare earth element decrease. More explanations are given in the next subsection of this paper.

HTXRD measurements make it possible to determine the NdPO$_4$ lattice parameters (a, b, c and β) coefficients of thermal expansion. Evolutions of lattice parameters (in Å) of the crystal cell against temperature (in K) are expressed by Eqs. (8)–(10):

$$a(T) = 6.738 + 6.268 \cdot 10^{-5} T \quad (8)$$

$$b(T) = 6.951 + 5.386 \cdot 10^{-5} T \quad (9)$$
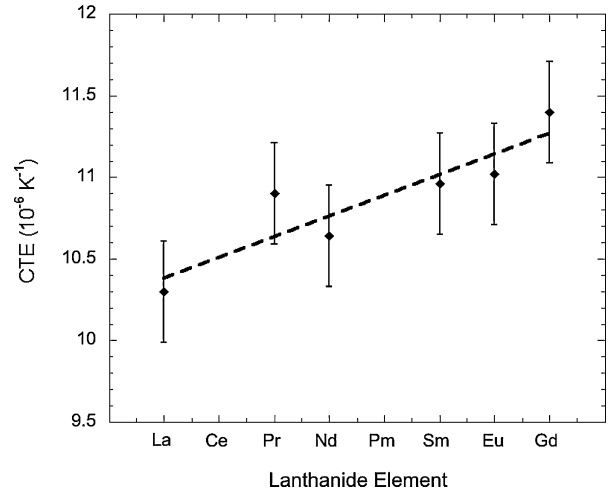
$$c(T) = 6.406 + 7.168 \cdot 10^{-5} T \quad (10)$$

Fig. 2. Coefficient of thermal expansion of LnPO$_4$ (Ln = La to Gd). Dotted line gives an indication of the CTE evolution with the lanthanide element.

β seems to be constant with temperature. Fig. 3 represents the thermal expansion of the lattice parameters (M), compared to their values at 25 °C (M_0). Eqs. (8)–(10) point out an anisotropic thermal expansion of NdPO$_4$, as the smallest cell parameter (c) has the highest coefficient of thermal expansion, and the difference with the largest parameter (a) is approximately 1×10^{-5} K^{-1} ($\approx 10\%$). This observation is interesting, as LnPO$_4$ CTE increases when the lanthanide ionic radius, and so when the atomic bend length, decreases. The CTE depends on the inter-atomic potential, as it is a macroscopic consequence of the potential well dissymmetry (see Fig. 4). In the case of the monazite structure, the narrower the potential well (or the smaller the atomic bond length), the greater the dissymmetry is, and so higher the CTE is.

The heat capacity data have been fitted to a polynomial function between 30 and 200 °C. The function is given by Eq. (11) and its coefficients have been collected in Table 1.

$$C_p(T) = \frac{a_{-1}}{T} + a_0 + a_1 \times T + a_2 \times T^2 + a_3 \times T^3 \quad (11)$$
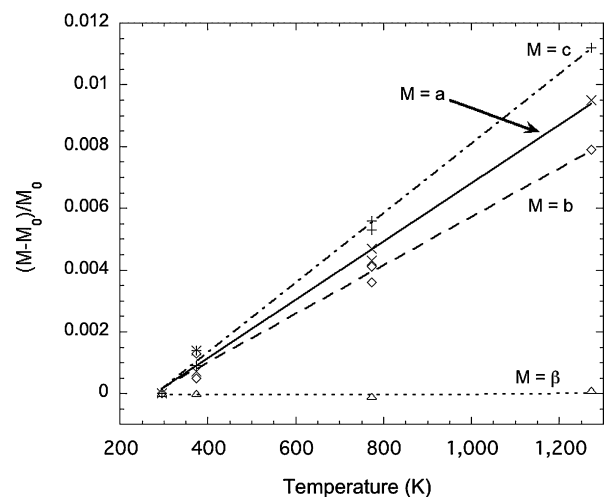

Fig. 3. Thermal expansion of NdPO$_4$ lattice parameters in the 100–1000 °C temperature range: $a_0 = 0.6735$ nm, $b_0 = 0.6950$ nm, $c_0 = 0.6405$ nm and $\beta = 103.68°$ (from JCPDS 83–0654).

Table 1
Coefficients of the polynomial fit (Eq. (11)) of the LnPO$_4$ (Ln = La to Gd) specific heat versus temperature

| | Specific heat $C_p(T)$ (J g^{-1} K^{-1}), T in °C | | | | | C_p at 50 °C | |
| | $C_p(T) = (a_{-1}/T) + a_0 + (a_1 \times T) + (a_2 \times T^2) + (a_3 \times T^3)$ | | | | | (J kg^{-1} K^{-1}) | J mol^{-1} K^{-1} |
	a_{-1}	$a_0 \times 10$	$a_1 \times 10^4$	$a_2 \times 10^6$	$a_3 \times 10^8$		
La		4.14	8.40	−1.50		452	106
Ce		4.34	7.51	−1.18		468	110
Pr		4.20	8.56	−1.57		458	108
Nd	−2.19	5.15	−7.98	9.43	−2.67	451	108
Sm		4.13	9.70	−1.95		456	112
Eu		4.28	7.74	−1.17		453	112
Gd		3.80	7.73	−1.24		415	105

From Eq. (11) and Table 1, heat capacities at 50 °C for LnPO$_4$ are calculated to be 106, 110, 108, 108, 112, 112 and 105 J mol^{-1} K^{-1} (for Ln = La, Ce, Pr, Nd, Sm, Eu and Gd, respectively). Those values are in good agreement with the work of Thiriet and Popa.[19,20] For comparison, the specific heat is 794 J mol^{-1} K^{-1} for britholite.[17] It can be highlighted that LaPO$_4$ and GdPO$_4$ heat capacities are lower than other LnPO$_4$ ones. The heat capacity of LnPO$_4$ has been previously described[19,20] as the sum of a lattice and an excess component. For LaPO$_4$ and GdPO$_4$, the heat capacity only depends on the lattice term, because of the configuration of the external electronic layer of the lanthanide, which is 4f^0 (empty) for La and 4f^7 (half-filled) for Gd. For the other lanthanide phosphates, the heat capacity is higher, due to the existence of the electronic term.

For the studied lanthanide elements, values of the dense material thermal conductivity λ_d (obtained from Eq. (2)) have been reported against the number of grain boundaries. Experimental plots are given in Fig. 5, and values of single crystal thermal conductivity λ_{sc} and grain boundary thermal resistance R_{gb} are reported in Table 2. The influence of the lanthanide element on λ_{sc} does not seem to be important. The grain boundaries thermal resistances are in the same range of values for the different lanthanide elements. This implies that the grain boundaries of the different compounds have a similar behavior, which was expected, as for any LnPO$_4$ compound no secondary phases se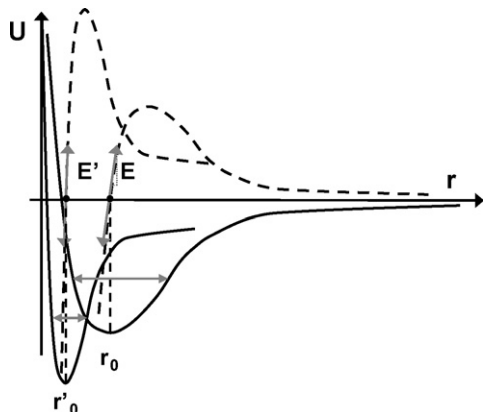gregated at the grain boundaries have been detected by XRD analysis and BSE-SEM observations. Nevertheless, the values of 8×10^{-7} m^2 K W^{-1} for grain boundary resistance seem rather high compared to those observed for oxides such as SnO$_2$ and Al$_2$O$_3$ (1–2 × 10^{-7} × m^2 K W^{-1}).[21]

3.2. Mechanical properties

The elastic properties of LnPO$_4$, considered as an isotropic, linearly elastic, solid material have been characterized by measurement of longitudinal and transverse ultrasonic wave velocities. E, G and ν for LnPO$_4$ (Ln = La, Pr, Nd or Eu) have been calculated using Eqs. (4)–(6). Experimental data of the elastic moduli are shown in Fig. 6. This figure points out that elastic moduli decrease with an increasing volume fraction of porosity. Several empirical models have been proposed to analyse relationships between elastic moduli and porosity.[22] The following equations describe the two models used for this study:

$$M = M_0(1 - hP) \tag{12}$$

$$M = M_0 \exp(-bP) \tag{13}$$

Fig. 4. Interaction potential vs. the inter-atomic distance.
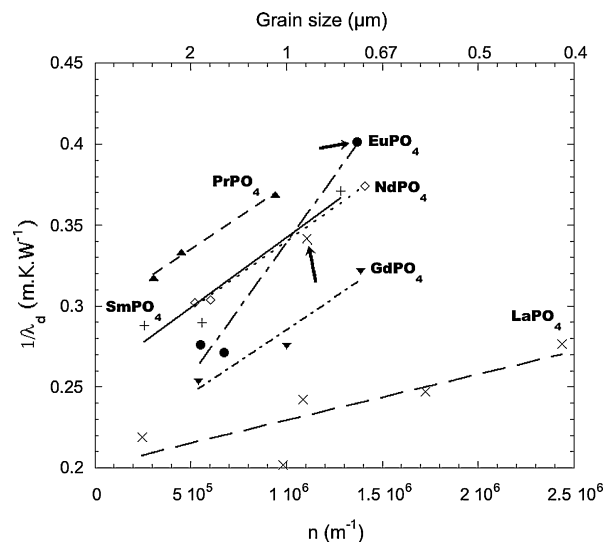

Fig. 5. Evolution of $1/\lambda_d$ vs. the number of grain boundaries crossed by the heat flow (i.e. the inverse of average grain size). Lines represent the linear regressions for the different lanthanide elements, and slopes are the grain boundaries thermal resistances. Arrows indicate two experimental points which seem to be false.

Table 2
Thermal and mechanical properties of LnPO$_4$ (Ln = La to Gd)

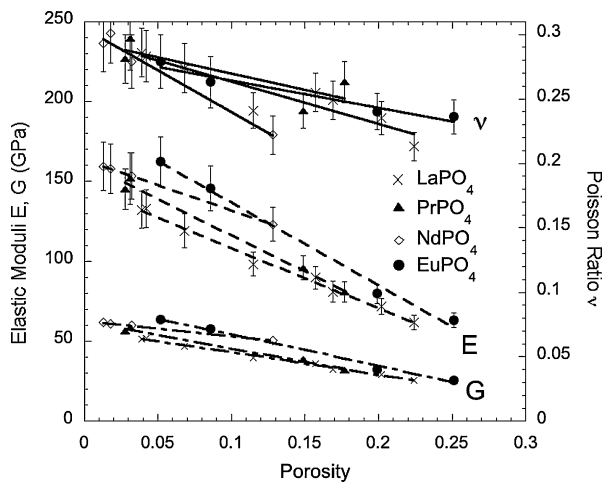| Lanthanide	La	Ce	Pr	Nd	Sm	Eu	Gd
α_m (10^{-6} K^{-1})	10.3 ± 0.5	–	10.9 ± 0.5	10.7 ± 0.5	11.0 ± 0.5	11.1 ± 0.5	11.4 ± 0.5
C_p(50 °C) (J K^{-1} mol^{-1})	102	110	104	108	112	110	105
λ_{sc} (W m^{-1} K^{-1})	5.3	–	3.4	4.4	3.9	5.8	4.8
R_{gb} (m^2 K W^{-1})	2.9×10^{-8}	–	7.9×10^{-8}	7.5×10^{-8}	8.7×10^{-8}	1.7×10^{-7}	8.0×10^{-8}
E_0 (GPa)	151 ± 7	–	164 ± 4	164 ± 1	–	202 ± 18	–
G_0 (GPa)	58 ± 3	–	64 ± 1	63 ± 0.5	–	79 ± 7	–
ν_0	0.298 ± 2.10^{-3}	–	0.307 ± 2.10^{-3}	0.286 ± 2.10^{-3}	–	0.295 ± 2.10^{-3}	–
σ_{r0} (MPa)	109	–	94	122	–	99	–
R (K)	49.1	–	36.4	49.6	–	31.1	–

Fig. 6. Experimental values of elastic moduli for LnPO$_4$ (Ln = La, Pr, Nd or Eu).

where M and M_0 represent the modulus of porous and dense materials, respectively. P is the volume fraction of porosity, and h and b are constants determined by data fitting. Eqs. (12) and (13) have been used because they show a valid data fit in our range of porosity (<40%).[23] Table 3 presents the results of the fits. ν_{calc} represent Poisson's ratio calculated from E_0 and G_0. The two models show good experimental fits, as R^2 is always higher than 0.98. The values of M_0 calculated from the two empirical models are a little different, but it has previously been reported that Eq. (13) had a tendency to over-estimate M_0, and Eq. (12) to under-estimate M_0.[23] Average values of M_0 have been calculated and are presented in Table 2. Young's moduli of dense LnPO$_4$ typically fall in the range 150–200 GPa, depending on the lanthanide

element: E_0 increases when the atomic number of the lanthanide element increases. It is of interest to notice that the CTE and the Young's modulus follows the same evolution with respect to the lanthanide element. Indeed, as the CTE, the Young's modulus is a consequence of inter-atomic potential: E depends on the second derivate of the potential curve at the equilibrium position (see Fig. 4). Experimental observations lead to the hypothesis that, in the case of monazite structure, a narrow potential well (obtained for a small ionic radius) has for consequence both a high Young's modulus and high CTE. The values of elastic moduli determined by this study are bigger than the ones determined by Morgan,[9] but the elaboration techniques are different and the microstructure is not precisely described. Compared to other materials of same interest such as britholite, LnPO$_4$ Young's moduli are higher,[17] but in the same range of values.

Fig. 7 shows the evolution of LaPO$_4$ flexural strength against the average grain size. Evolution of density against grain size is also exposed. The maximal flexural strength ($\sigma_f = 104 \pm 12$ MPa) is obtained for a fine grain size and dense material. This value is indicative of a brittle behavior of LaPO$_4$. PrPO$_4$, NdPO$_4$ and EuPO$_4$ flexural strengths follow the same behavior at constant porosity. Flexural strength decreases with increasing grain size. It can be explained by the size of the coarsest grains that control the failure of dense polycrystalline ceramics. Dependence of fracture strength versus grain size can be expressed by the following law[23]:

$$\sigma_f = Ad^a \qquad (14)$$

where d is the average grain size, A and a are two experimental constants ($0.2 \leq a \leq 0.9$). No fit of Eq. (14) to the experimental data was performed, because of a lack of experimental data and

Table 3
Fit parameters of the evolution of the elastic moduli of LnPO$_4$ vs. porosity

| Model	Ln	E_0 (GPa)	b	R^2	G_0 (GPa)	b	R^2	ν_0	b	R^2	ν_0 Calculated
$M = M_0(1 - bP)$	La	146	2.573	0.992	57	2.459	0.995	0.296	1.103	0.869	0.288
	Nd	164	1.936	1.000	63	1.543	0.998	0.305	2.147	0.974	0.303
	Eu	189	2.744	0.992	74	2.691	0.992	0.285	0.734	0.944	0.277
	Pr	162	2.784	0.990	63	2.679	0.991	0.295	0.851	0.670	0.293
$M = M_0 e^{-bP}$	La	156	3.917	0.988	60	3.656	0.990	0.299	1.292	0.856	0.297
	Nd	165	2.268	1.000	63	1.747	0.997	0.308	2.558	0.981	0.306
	Eu	215	4.901	0.997	84	4.734	0.996	0.286	0.820	0.951	0.286
	Pr	167	3.945	0.988	65	3.747	0.983	0.295	0.929	0.658	0.295
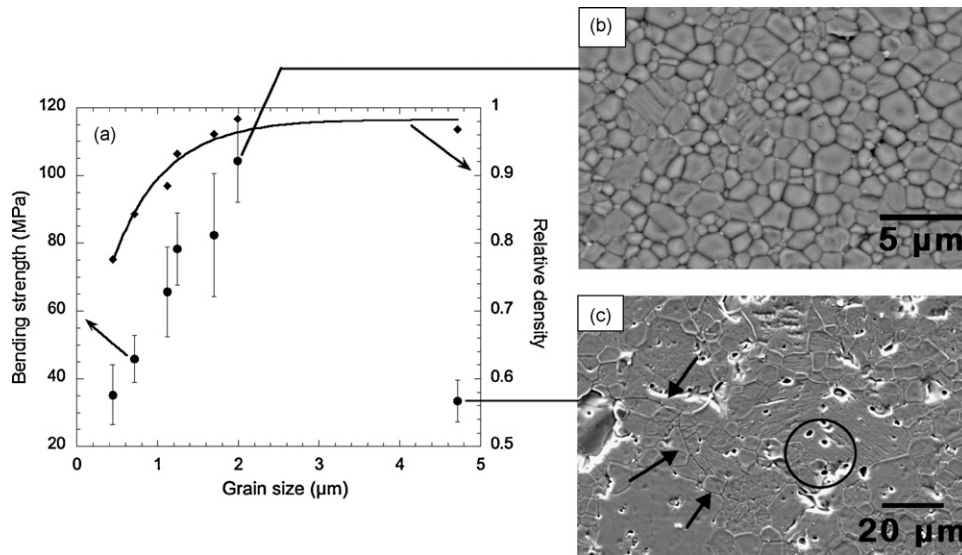
Fig. 7. (a) Flexural strength of LaPO$_4$ and relative density against grain size. (b) Optimal microstructure (relative density, 98.3%; grain size, 1.99 μm) for which the flexural strength is maximum. (c) Coarse grained sample (relative density, 96.8%; grain size, 4.71 μm) with low fracture strength due to the presence of intragranular pores and micro-cracks.

the grain size range was not broad enough to permit good calculations. In the case of porous materials, the pores that constitute the critical defects govern fracture. Evolution of fracture strength against porosity can be described by a classical expression:

$$\sigma_f = \sigma_0 \exp(-bP) \tag{15}$$

where σ_0 is the extrapolated flexural strength for a totally dense material, b the experimental constant and P is the porosity ratio. Results from Eq. (15) fitted to the experimental data are given in Table 4. Only LaPO$_4$ flexural strength data show a good fit with Eq. (15). The low values of R^2 for the three other compounds can be explained by the relative lack of experimental data. However, it is remarkable that the values of σ_0 are not so different for the four-studied LnPO$_4$. For comparison, britholite maximal flexural strength is about 80 MPa,[17] and hydroxyapatite one is 135 MPa.[18]

SEM examination of the fracture surfaces (Fig. 8) revealed the presence of both intergranular (circle) and intragranular (dotted circle) cracks. It proves that the crack propagation occurs according to a mixed mode of failure.

Micro-indentation experiments pointed out the extreme brittleness of those compounds. Indeed, it was very difficult to obtain indents permitting H_V and K_{Ic} calculations. Excessive chipping occurred, and generally invalidated the calculation. Nevertheless, some indents were good enough to permit crack measurement and then fracture toughness determination. For LnPO$_4$ (Ln = La, Pr, Nd or Eu), only six dense samples

have been characterized, and showed a Vickers Hardness of approximately 5.0 ± 0.5 GPa and a fracture toughness around 1 ± 0.1 MPa m$^{1/2}$. The values determined by this study are just first indications of the real values, as not enough samples had been characterized for a good statistical study. However, those values are in accordance with previous works.[8–10] The other potential minor actinides host matrices exhibit similar values for fracture toughness ($K_{Ic(britholite)} = 0.75$ MPa m$^{1/2}$,[17] and $K_{Ic(hydroxyapatite)} = 1.2$ MPa m$^{1/2}$,[18]).

From the previous results, it was possible to determine the first parameter of thermal shock resistance, R, which represents the theoretical instantaneous difference of temperature required to initiate cracks in the material.
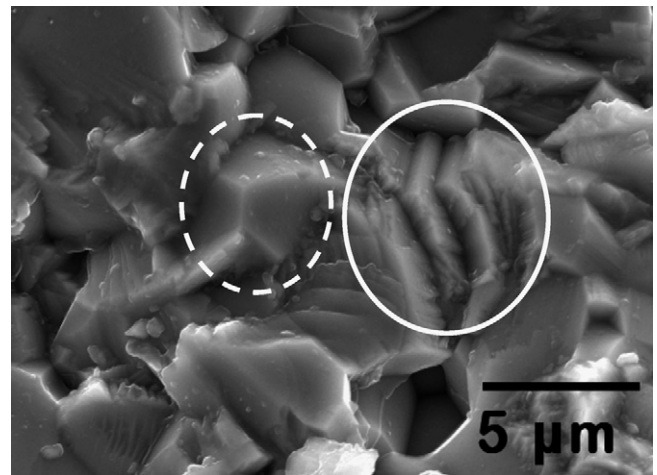
$$R = \frac{\sigma_f(1 - \nu)}{\alpha E} \tag{16}$$

Fig. 8. SEM micrograph of a NdPO$_4$ sample (relative density, 98.6%; grain size, 2.59 μm). Transgranular fracture typical steps and grains prints indicating intergranular fracture are visible on the picture.

Table 4
Results of experimental fit of flexural strength vs. porosity

Lanthanide		La	Pr	Nd	Eu
$\sigma_f = \sigma_0 \exp(-bP)$	σ_0 (MPa)	109	94	122	99
	b	5.09	3.69	2.47	2.37
	R^2	0.98	0.94	0.88	0.83

R values are summarized in Table 2. For LnPO$_4$ (Ln = La, Pr, Nd or Eu), R is in between 30 and 50 °C. It means that monazite is not thermal shock resistant since it cannot support a temperature variation higher than 50 °C without cracking.

4. Conclusions

The thermal and mechanical properties of LnPO$_4$ (Ln = La to Gd), a potential host matrix for minor actinides immobilization, have been measured as a function of the microstructure. From a mechanical point of view, monazite showed a brittle behavior ($\sigma_f < 130$ MPa) associated to low fracture toughness (about 1 MPa m$^{1/2}$). This brittle behavior made the micro-indentation analyses very imprecise, due to major chipping of the material. Perhaps the macro-indentation technique would be more appropriate in that case. LnPO$_4$ Young's modulus (founded to be in between 150 and 200 GPa) and the coefficient of thermal expansion ($\approx 9.5 \times 10^{-6}$ K^{-1}), increase with an increasing atomic number of the lanthanide element. We could show that porosity plays an important role in both thermal and mechanical properties. For example, the flexural strength is divided by three for materials with density of 98% to 60% of the theoretical density, respectively. The relatively high value of the coefficient of thermal expansion, associated with the low mechanical properties, induces a weak resistance to thermal shocks. In a view of using the material as a nuclear waste matrix, the low thermal conductivity and the high specific heat of LnPO$_4$ limit the temperature rising associated with the nuclear disintegration of radionuclides, but also limit the annealing of irradiation defects by temperature.

Acknowledgments

References

1. *J. Officiel de la République Française*, 1992, 10–12.
2. Guy, C., Audubert, F., Lartigue, J.-E., Latrille, C., Advocat, T. and Fillet, C., *C.R. Phys.*, 2002, **3**, 827–837.
3. Trocellier, P., *Ann. Chim. Sci. Mater.*, 2000, **25**, 321–337.
4. Beall, G. W. and Boatner, L. A., *J. Inorg. Nucl. Chem.*, 1981, **43**, 101–105.
5. Ewing, R. C. and Haaker, R. F., *Nucl. Chem. Waste Manage.*, 1980, **1**, 51–57.
6. Karioris, F. G., *Radiat. Eff. Lett.*, 1981, **58**(1–2), 1–3.
7. Poitrasson, F., *Geochim. Cosmochim. Acta*, 2004, **68**(10), 2207–2221.
8. Lucas, S., Ph.D. thesis, Université de Limoges, 2003.
9. Morgan, P. E. D. and Marshall, D. B., *J. Am. Ceram. Soc.*, 1995, **78**(6), 1553–1563.
10. Hikichi, Y., Ota, T. and Hattori, T., *Mineral. J.*, 1997, **19**(3), 123–130.
11. Thiriet, C., Konings, R. J. M., Javorsky, P., Magnani, N. and Wastin, F., *J. Chem. Thermodyn.*, 2005, **37**, 131–139.
12. Bregiroux, D., Ph.D. thesis, Université de Limoges, 2005.
13. Grandjean, S., Ph.D. thesis, Université de Limoges, 2002.
14. Degiovanni, A., *Rev. Gén. Therm. Fr.*, 1977, **185**, 420–441.
15. Smith, D. S., Grandjean, S., Absi, J., Kadiebu, S. and Fayette, S., *High Temp.-High Press.*, 2003, **35/36**, 93–99.
16. Evans, A. C. and Charles, E. A., *J. Am. Ceram. Soc.*, 1976, **59**(7–8), 371–372.
17. Bregiroux, D., Audubert, F., Champion, E. and Bernache-Assollant, D., *Mater. Lett.*, 2003, **57**, 3526–3531.
18. Halouani, R., Bernache-Assollant, D., Champion, E. and Ababou, A., *J. Mater. Sci.: Mater. Med.*, 1994, **5**, 563–568.
19. Thiriet, C., Konings, R. J. M., Javorsky, P. and Wastin, F., *Phys. Chem. Miner.*, 2004, **31**, 347–352.
20. Popa, K., Konings, R. J. M. and Geisler, T., *J. Chem. Thermodyn.*, 2007, **39**(2), 236–239.
21. Smith, D. S., Grandjean, S., Absi, J., Kadiebu, S. and Fayette, S., *J. Am. Ceram. Soc.*, 2003, **86**(1), 105–111.
22. Dean, E. A. and Lopez, J. A., *J. Am. Ceram. Soc.*, 1983, **66**(5), 366–370.
23. Knudsen, F. P., *J. Am. Ceram. Soc.*, 1959, **42**(8), 376–387.